HOKKAIDO UNIVERSITY

Title	Accurate and efficient computation of the 3D radiative transfer equation in highly forward-peaked scattering media using a renormalization approach
Author(s)	Fujii, Hiroyuki; Yamada, Yukio; Chiba, Go; Hoshi, Yoko; Kobayashi, Kazumichi; Watanabe, Masao
Citation	Journal of Computational Physics, 374, 591-604 https://doi.org/10.1016/j.jcp.2018.07.047
Issue Date	2018-12-01
Doc URL	http://hdl.handle.net/2115/79910
Rights	© 2018. This manuscript version is made available under the CC-BY-NC-ND 4.0 license https://creativecommons.org/licenses/by-nc-nd/4.0/
Rights(URL)	https://creativecommons.org/licenses/by-nc-nd/4.0/
Type	article (author version)
File Information	JCP_Fujii.pdf

Instructions for use

Hokkaido University Collection of Scholarly and Academic Papers : HUSCAP

Contents lists available at ScienceDirect

Journal of Computational Physics

journal homepage: www.elsevier.com/locate/jcp

Accurate and efficient computation of the 3D radiative transfer equation in highly forward-peaked scattering media using a renormalization approach

Hiroyuki Fujii[a,*], Yukio Yamada[b], Go Chiba[c], Yoko Hoshi[d], Kazumichi Kobayashi[a], Masao Watanabe[a]

[a]*Division of Mechanical and Space Engineering, Faculty of Engineering, Hokkaido University, Kita 13 Nishi 8, Kita-ku, Sapporo, Hokkaido 060-8628, Japan*
[b]*Brain Science Inspired Life Support Research Center, University of Electro-Communications, 1-5-1 Chofugaoka, Chofu, Tokyo 182-8585, Japan*
[c]*Division of Energy and Environmental Systems, Faculty of Engineering, Hokkaido University, Kita 13 Nishi 8, Kita-ku, Sapporo, Hokkaido 060-8628, Japan*
[d]*Preeminent Medical Photonics Education & Reseach Center, Hamamatsu University School of Medicine, 1-20-1 Handayama, Higashi-ku, Hamamatsu, Sizuoka 431-3192, Japan*

ARTICLE INFO

Article history:

Keywords: Radiative transfer equation, Discrete ordinates method, Highly forward-peaked scattering phase function, Renormalization approach, Double-exponential formula

ABSTRACT

This paper considers an accurate and efficient numerical scheme for solving the radiative transfer equation (RTE) based on the discrete ordinates method (DOM) in highly forward-peaked scattering media. The DOM approximates the scattering integral of the RTE including the phase function into a quadrature sum with the total number of discrete angular directions (TND) by a quadrature set. Due to large numerical errors of the scattering integral based on the DOM in highly forward-peaked scattering, the phase function is renormalized to satisfy its normalization conditions. Although the renormalization approaches of the phase function improve the accuracy of the numerical results of the RTE, the computational efficiency of the RTE is still required. This paper develops the first order renormalization approach using the double exponential formula for three quadrature sets: level symmetric even, even and odd, and Lebedev sets in a wide range of the TND from 48 to 1454. Numerical errors of the three-dimensional time-dependent RTE are investigated by the analytical solutions of the RTE. The investigation shows that the level symmetric even set with the TND of 48 using the developed approach provides the most accurate results of the RTE among the quadrature sets in the range of the TND, while to obtain the same accuracy by the conventional zeroth order renormalization approach, the TND needs to be larger than 360. The results suggest the large reduction of computational loads by the developed approach to less than 10 percent from those in the conventional approach.

© 2020 Elsevier Inc. All rights reserved.

*Corresponding author

1. Introduction

Linear transport equation or linear Boltzmann equation in a random medium has been encountered in various engineering and scientific fields such as biomedical optics based on radiative transfer, and nuclear reactor physics based on neutron transport (Case, Kenneth and Zweifel, P, 1967). Especially, the radiative transfer equation (RTE) attracted great interests in recent ten years because of the possibility as a forward model to describe photon migration in biological tissue for optical computed tomography (diffuse optical tomography) (Gibson et al., 2005; Yamada and Okawa, 2014), which has a potential to enable *in-vivo* imaging of various organs and tissue volumes such as lung (Kannan, R. and Przekwas, 2011) and brain (Kannan and Przekwas, 2012) by irradiating near-infrared light in the wavelength range from 700 nm to 1000 nm. Nevertheless, few groups in this field investigate the RTE-based optical tomography now, because it is quite difficult to solve the RTE analytically or numerically. Although analytical solutions of the RTE are given for simple geometries (Markel, 2004; Machida et al., 2010; Liemert and Kienle, 2012) such as infinitely extended homogeneous media, it is not realistic to pursue analytical solutions for heterogeneous media like animal and human bodies. Also, an accurate and efficient numerical solver of the RTE is requested because of its more complex algorithm and higher computational loads than the diffusion approximation (DA) and Monte Carlo simulations with the help of graphics processing units.

In numerical calculation of the RTE, it is necessary to discretize the spatial, angular, and temporal variables because the RTE is an integro-differential equation for the multi-variable function of the light intensity. To attain the accuracy of the numerical solution of the RTE, fast convergence of the numerical calculation of the scattering integral with respect to the total number of discrete angular directions is crucial. Here, ”convergence” means that the numerical integration approaches toward a theoretical value when the total number increases, and ”fast convergence” means that the numerical integration approaches to the theoretical value at a small total number of discrete angular directions. The discrete ordinates method (DOM) (Chandrasekhar, 1960; Carlson and Lee, 1961) is one of the gold standards for angular discretization (Hardy et al., 2017), which approximates the scattering integral into a quadrature sum by a quadrature set. It is known that the photon migration in biological tissue undergoes highly forward-peaked scattering with the anisotropic factor ranging from 0.8 to 1.0 approximately (Cheong et al., 1990) unlike the neutron transport, and the values of the phase function increase exponentially as the angle between the incident and scattered directions approaches to zero. This behavior of the phase function results in slow convergence of the scattering integral and large errors of the numerical solution of the RTE using the DOM.

To achieve fast convergence of the numerical calculation of the scattering integral for highly forward-peaked scattering, in the research field of charged-particle transport, the Galerkin quadrature method (Morel, 1989; Morel et al., 2017) and Boltzmann Fokker-Planck decomposition method (Landesman and Morel, 1989) have been developed, especially, to treat exactly the delta function scattering. On the other hand, in the field of biomedical optics or radiative heat transfer, approaches for renormalizing the phase function have been developed (Wiscombe, 1976; Liu et al., 2002; Boulet et al., 2007; Hunter and Guo, 2012). This paper focuses on the renormalization approach. The renormalization approaches have several formulations: the zeroth order renormalization approaches by early studies

(Wiscombe, 1976; Liu et al., 2002) to satisfy the zeroth order normalization condition of the phase function; and the first order renormalization approach in implicit forms by Hunter and Guo (Hunter and Guo, 2012) to satisfy the zeroth and first order normalization conditions. Recently, the authors have developed the first order approach in the explicit form using the double exponential formula (DEF) for the quadrature set based on the extended trapezoidal rule (ETR) (Fujii et al., 2016). The approach developed in the previous paper (Fujii et al., 2016) can reduce numerical errors of the scattering integral and improve the accuracy of the numerical solution of the RTE compared with the zeroth order renormalization approach in a range of the total numbers of discrete angular directions for the ETR set. Also, the previous paper has shown that the total number needs to be more than 480 for the accurate numerical results of the RTE. Despite the large reduction of the numerical errors by the previously developed approach based on the ETR set, the necessity of the total number being larger than 480 still leads to high computation loads, and a further reduction of computation loads is required. In the renormalization approach, a choice of the quadrature set is crucial because the quadrature set strongly influences the numerical results of the RTE even when the same renormalization approach is used. The strong influence has motivated this study to examine the compatibility of the renormalization approaches for various quadrature sets in a wide range of the total number, and to explore an accurate and efficient quadrature set.

This paper develops the first order renormalization approach using the DEF in three kinds of quadrature sets: the level symmetric even, even and odd, and Lebedev quadrature sets with the two cases of highly forward-peaked scattering, and investigates the numerical errors of the scattering integral and numerical solution of the RTE. Then, an accurate and efficient quadrature set using the first order renormalization approach is recommended. Furthermore, the developed approach with the recommended quadrature set is tested for accuracy and efficiency by comparing with the Galerkin quadrature method.

The following section describes the RTE and scattering integral, the conventional and developed approaches for the renormalization of the phase function, a method of numerical calculation of the time-dependent RTE for a three dimensional scattering medium using the DOM and finite difference method, and measurement quantities and numerical conditions. Section 3 provides the numerical results for verification of the developed approach, and the comparison study of the numerical errors between the developed approach and the Galerkin quadrature method. Finally, conclusions are described. Appendix outlines the formulation of the Galerkin quadrature method.

2. The photon migration theory and numerical method of the RTE

2.1. The RTE and scattering integral

The time-dependent RTE is formulated in three dimensions (3D) as (Chandrasekhar, 1960),

$$\left[\frac{\partial}{v\partial t} + \boldsymbol{\Omega}\cdot\nabla + \mu_a(\boldsymbol{r}) + \mu_s(\boldsymbol{r})\right] I(\boldsymbol{r},\boldsymbol{\Omega},t) = \mu_s(\boldsymbol{r})\int_{4\pi} d\boldsymbol{\Omega}'\; p(\boldsymbol{\Omega},\boldsymbol{\Omega}')I(\boldsymbol{r},\boldsymbol{\Omega}',t) + q(\boldsymbol{r},\boldsymbol{\Omega},t), \tag{1}$$

where $I(\boldsymbol{r},\boldsymbol{\Omega},t)$ in $\mathrm{Wcm^{-2}\ sr^{-1}}$ represents the light intensity as a function of spatial location $\boldsymbol{r} = (x, y, z)$ in cm for a 3D Cartesian coordinate system, angular direction (unit direction vector) $\boldsymbol{\Omega} = (\Omega_x, \Omega_y, \Omega_z) = (\sin\theta\cos\phi, \sin\theta\sin\phi, \cos\theta)$ (polar angle, $\theta \in [0, \pi]$, azimuthal angle, $\phi \in [0, 2\pi]$ in sr), and time t in ps. $\mu_a(\boldsymbol{r})$ and $\mu_s(\boldsymbol{r})$ in $\mathrm{cm^{-1}}$ are the absorption

and scattering coefficients, respectively, v is the speed of light in the medium, $p(\mathbf{\Omega}, \mathbf{\Omega}')$ in sr^{-1} is the phase function, and $q(\boldsymbol{r}, \mathbf{\Omega}, t)$ in Wcm^{-2} sr^{-1} is a source function.

The phase function, $p(\mathbf{\Omega}, \mathbf{\Omega}')$, represents a probability of single scattering with the change in the direction from the incident direction, $\mathbf{\Omega}'$, to the scattered direction, $\mathbf{\Omega}$. Here, the phase function is assumed to be dependent only on the polar scattering angle, $\varphi = \cos^{-1} \mathbf{\Omega} \cdot \mathbf{\Omega}'$, resulting in $p(\mathbf{\Omega}, \mathbf{\Omega}') = p(\mathbf{\Omega} \cdot \mathbf{\Omega}')$. For the formulation of $p(\mathbf{\Omega} \cdot \mathbf{\Omega}')$, the Henyey-Greenstein phase function (Henyey and Greenstein, 1941) is widely employed,

$$p(\mathbf{\Omega} \cdot \mathbf{\Omega}') = \frac{1}{4\pi} \frac{1 - g^2}{(1 + g^2 - 2g\mathbf{\Omega} \cdot \mathbf{\Omega}')^{3/2}}, \tag{2}$$

where $g \in [-1, 1]$ represents the anisotropic factor, defined by

$$g = \frac{\int_{4\pi} d\mathbf{\Omega}' \; p(\mathbf{\Omega} \cdot \mathbf{\Omega}') \mathbf{\Omega} \cdot \mathbf{\Omega}'}{\int_{4\pi} d\mathbf{\Omega}' \; p(\mathbf{\Omega} \cdot \mathbf{\Omega}')}. \tag{3}$$

While scattering in neutron transport can be treated as isotropic ($g = 0.0$) or weakly anisotropic ($-0.5 \lesssim g \lesssim 0.5$), photon migration in biological tissue undergoes highly forward-peaked scattering ($0.8 \lesssim g \lesssim 1.0$) (Cheong et al., 1990).

The scattering integral (first term of the right hand side of Eq. (1)) describes energy gain of photons by scattering, and this term is approximated by the DOM as a quadrature sum,

$$\mu_s(\boldsymbol{r}) \int_{4\pi} d\mathbf{\Omega}' \; p(\mathbf{\Omega} \cdot \mathbf{\Omega}') I(\boldsymbol{r}, \mathbf{\Omega}', t) \sim \mu_s(\boldsymbol{r}) \sum_{l'=1}^{N_\Omega} w_{l'} p_{ll'} I_{l'}(\boldsymbol{r}, \mathbf{\Omega}_{l'}, t), \tag{4}$$

where $w_{l'}$ is a weight for numerical integration; $p_{ll'}$, $\mathbf{\Omega}_{l'}$, and $I_{l'}$ are discrete forms of p, $\mathbf{\Omega}$, and I, respectively; N_Ω is a total number of discrete angular directions; the subscripts l' and $l \in [1, 2, \cdots N_\Omega]$ denote the indices of the discrete angular directions of the incident and scattered light, respectively.

In the DOM, a quadrature set of $(w_l, \mathbf{\Omega}_l)$ should be given appropriately. Although many kinds of quadrature sets for the DOM have been developed mainly in the field of the neutron transport (Fiveland, 1991; Carlson, 1971; Balsara, 2001), the most common choice is the level symmetric even (LSE) quadrature set (Fiveland, 1991). The LSE set is determined to satisfy the even-moment conditions, and invariant with respect to 90-degree axis rotation and line reflection. Figure 1(a) shows an example of the distribution of $(w_l, \mathbf{\Omega}_l)$ for the LSE set with $N_\Omega = 288$ in the first octant, where circles and colors represent $\mathbf{\Omega}_l$ and w_l, respectively, and the values of $\mathbf{\Omega}_l$ and w_l are calculated by referring to the original paper (Fiveland, 1991). Recently, the even and odd (EO) quadrature set is developed to satisfy both the even- and odd-moment conditions (Endo and Yamamoto, 2007) (the distribution with $N_\Omega = 288$ is plotted in Fig. 1(b)). The LSE and EO sets have limitations on N_Ω under the condition that w_l is positive, i.e., maximum values of N_Ω are 360 and 288 for the LSE and for the EO sets, respectively. On the other hand, it has been reported in (Gregersen and York, 2005; Sanchez, 2012; Long et al., 2016) that the Lebedev quadrature set can provide the same accuracy as the LSE set and at the same time reduce computation loads to two-thirds of that by the LSE set. The Lebedev quadrature set is determined based on the spherical harmonics expansions to satisfy the invariance under

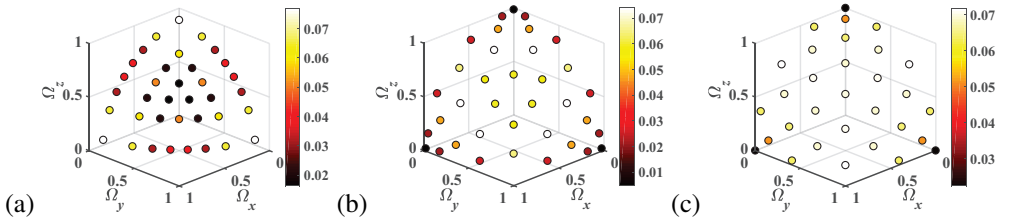

Fig. 1. Distributions of the quadrature sets of $(w_l, \mathbf{\Omega}_l)$ in the first octant; (a) the LSE set with $N_\Omega = 288$, (b) EO set with $N_\Omega = 288$, and (c) Lebedev set with $N_\Omega = 194$. Circles and colors represent $\mathbf{\Omega}_l$ and w_l, respectively. Calculations of $(w_l, \mathbf{\Omega}_l)$ refer to the original papers: (Fiveland, 1991) for the LSE set, (Endo and Yamamoto, 2007) for the EO set, and (Lebedev, 1975, 1977) for the Lebedev set.

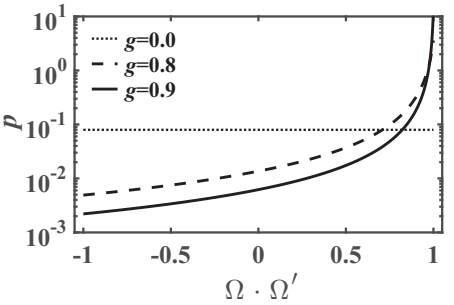

Fig. 2. Henyey-Greenstein phase function as a function of $\mathbf{\Omega} \cdot \mathbf{\Omega}' = \cos\varphi$ for isotropic scattering ($g = 0.0$), and highy forward-peaked scattering ($g = 0.8$ and 0.9), in a logarithmic scale.

the octahedra group with its maximum value of N_Ω as large as 5808 (Lebedev, 1975, 1977) (the distribution with $N_\Omega = 194$ is plotted in Fig. 1(c)).

The above quadrature sets are given without considering the behavior of the phase function, $p(\mathbf{\Omega} \cdot \mathbf{\Omega}')$, which characterizes anisotropy of scattering. The Henyey-Greenstein phase function (Eq. (2)) is plotted in Fig. 2 as a function of $\mathbf{\Omega} \cdot \mathbf{\Omega}' \in [-1, 1]$ or $\cos\varphi$ ($\varphi \in [0, \pi]$) in a logarithmic scale. For isotropic scattering ($g = 0.0$) like neutron transport, the phase function is constant over the whole domain of $\mathbf{\Omega} \cdot \mathbf{\Omega}'$. For highly forward-peaked scattering ($g = 0.8$ and 0.9) like photon migration in biological tissue, meanwhile, the phase function tends to increase exponentially as $\mathbf{\Omega} \cdot \mathbf{\Omega}'$ approaches to unity (φ approaches to 0). This feature of the phase function prevents fast convergence of calculation of the scattering integral (Eq. (4)) because N_Ω must increase for highly forward-peaked scattering.

2.2. Conventional approach for calculation of the scattering integral

To achieve fast convergence of the numerical calculation of the scattering integral for highly forward-peaked scattering, approaches for renormalizing the phase function have been developed (Wiscombe, 1976; Liu et al., 2002; Boulet et al., 2007; Hunter and Guo, 2012), as discussed in the following.

The Henyey-Greenstein phase function (Eq. (2)) can be expanded in the series of the Legendre polynomials,

$$p(\mathbf{\Omega} \cdot \mathbf{\Omega}') = \sum_{n=0}^{\infty} \frac{2n+1}{4\pi} g^n P_n(\mathbf{\Omega} \cdot \mathbf{\Omega}'), \tag{5}$$

where P_n is the (unassociated) Legendre polynomials of order $n \in \mathbb{N}$. From Eq. (5), the phase function satisfies the L-th order normalization conditions (L: nonnegative integer) for any nonzero value of g, in the following continuous and discrete forms:

$$g^{-L}\int_{4\pi} d\boldsymbol{\Omega}' p(\boldsymbol{\Omega}\cdot\boldsymbol{\Omega}')P_L(\boldsymbol{\Omega}\cdot\boldsymbol{\Omega}') \sim g^{-L}\sum_{l'=1}^{N_\Omega} w_{l'}\, p_{ll'} P_L(\boldsymbol{\Omega}_l\cdot\boldsymbol{\Omega}_{l'}) = 1, \qquad l = 1, 2, \cdots, N_\Omega. \tag{6}$$

It has been reported that for weakly anisotropic scattering, the normalization conditions are satisfied by the quadrature sets stated above, meanwhile for highly forward-peaked scattering the normalization conditions are not satisfied anymore. In the early studies, zeroth order renormalization approaches of the phase function have been developed in various formulations (Wiscombe, 1976; Liu et al., 2002). In these approaches, the renormalized phase function $\hat{p}_{ll'}$ is introduced to satisfy the zeroth order normalization condition; Eq. (6) with $L = 0$ and replacing $p_{ll'}$ by $\hat{p}_{ll'}$, i.e. $g^0 \sum_{l'=1}^{N_\Omega} w_{l'}\hat{p}_{ll'} P_0 = \sum_{l'=1}^{N_\Omega} w_{l'}\hat{p}_{ll'} = 1$. Among them, Liu's formulation (Liu et al., 2002) simply renormalizes the phase function as

$$\hat{p}_{ll'} = f_l p_{ll'}, \qquad f_l = \left[\sum_{l'=1}^{N_\Omega} w_{l'} p_{ll'}\right]^{-1}, \tag{7}$$

where f_l is a renormalizing factor. The zeroth order renormalization approach can improve the accuracy of numerical solutions of the RTE for highly forward-peaked scattering, but the higher order normalization condition of Eq. (6) with $L \geq 1$ is still unsatisfied even by introducing $\hat{p}_{ll'}$.

Recently, further improvement of the renormalization approach has been reported by Hunter and Guo (Hunter and Guo, 2012). In their approach, so called the first order renormalization approach with $L = 1$, the renormalized phase function is given by $\hat{p}_{ll'} = W_{ll'} p_{ll'}$, where $W_{ll'}$ represents the weight matrix determined by an inverse analysis so as to minimize the numerical errors of the zeroth and first order normalization conditions of Eq. (6) with $L = 0$ and 1 when replacing $p_{ll'}$ by $\hat{p}_{ll'}$. Because $W_{ll'}$ is determined implicitly under an ill-posed condition, the values of $W_{ll'}$ are dependent on the inverse model. On the other hand, an explicit determination of the weight matrix like Eq. (7) is convenient for examining the convergence of calculation of the scattering integral and useful for other researchers.

2.3. developed approach for calculation of the scattering integral

This paper develops the first order renormalization approach for the highly forward-peaked phase function expressed by the following equations:

$$\hat{p}_{ll'} = f_l W_{ll'} p_{ll'}, \qquad f_l = \left[\sum_{l'=1}^{N_\Omega} w_{l'} W_{ll'} p_{ll'}\right]^{-1}, \tag{8}$$

where $\hat{p}_{ll'}$ is again the renormalized phase function; and the renormalizing factor, f_l, is determined to satisfy the zeroth order normalization condition of Eq. (6) with $L = 0$ and replacing $p_{ll'}$ by $\hat{p}_{ll'}$, i.e. $\sum_{l'=1}^{N_\Omega} w_{l'}\hat{p}_{ll'} = 1$. The weight matrix, $W_{ll'}$, is given explicitly by the DEF,

$$W_{ll'} = \begin{cases} \dfrac{\cosh(u_{ll'})\exp[-2\sinh(u_{ll'})]}{\{\cosh[\sinh(u_{ll'})]\exp[-\sinh(u_{ll'})]\}^2} & |u_{ll'}| \leq u_{th} \\ \dfrac{\cosh(u_{th})\exp[-2\sinh(u_{th})]}{\{\cosh[\sinh(u_{th})]\exp[-\sinh(u_{th})]\}^2} & |u_{ll'}| > u_{th} \end{cases}, \tag{9}$$

where $u_{ll'} = \sinh^{-1}(\tanh^{-1}(\boldsymbol{\Omega}_l\cdot\boldsymbol{\Omega}_{l'}))$; and $u_{th}(>0)$ is a threshold of $u_{ll'}$ for calculation of $W_{ll'}$. As shown in Eq. (9), $W_{ll'}$ varies with $u_{ll'}$ when $|u_{ll'}| \leq u_{th}$, and is kept constant when $|u_{ll'}| > u_{th}$. Because our proposal employs the DEF

heuristically and empirically, u_{th} is not given theoretically unlike the original DEF (Takahasi and Mori, 1974; Mori and Sugihara, 2001). In the developed approach, u_{th} is determined by fitting so as to satisfy the first order normalization condition of Eq. (6) with $L = 1$ and replacing $p_{ll'}$ by $\hat{p}_{ll'}$ under a well-posed condition; that is, u_{th} is determined so that a numerical integral of $S_1^l = g^{-1} \sum_{l'=1}^{N_\Omega} w_{l'} \hat{p}_{ll'} \boldsymbol{\Omega}_l \cdot \boldsymbol{\Omega}_{l'}$ converges to its theoretical value of unity.

The renormalized phase function $\hat{p}_{ll'} = f_l W_{ll'} p_{ll'}$ is calculated by the following steps:

Step (i) *Selection of a quadrature set of* $(w_l, \boldsymbol{\Omega}_l)$ *and a phase function of* p: A quadrature set such as the LSE, EO, or Lebedev set is selected and values of $(w_l, \boldsymbol{\Omega}_l)$ refer to the original papers. Also, the phase function of p is selected and discretized as $p_{ll'}$ by using the selected quadrature set. In this study, the Henyey-Greenstein phase function (Eq. (2)) is used.

Step (ii) *Calculation of* $W_{ll'}$: $u_{ll'}$ is calculated from $\boldsymbol{\Omega}_l \cdot \boldsymbol{\Omega}_{l'}$ and u_{th} is given as 0.5 for the initial value or a value updated in Step (iv). Then, $W_{ll'}$ is calculated from Eq. (9).

Step (iii) *Calculation of* f_l *and* $\hat{p}_{ll'}$: f_l is calculated using the second equation of Eq. (8). Then, $\hat{p}_{ll'}$ is currently calculated using the first equation of Eq. (8).

Step (iv) *Updating of* u_{th}: To evaluate the first order normalization condition for the current values of $\hat{p}_{ll'}$, the average of S_1^l over $l = 1$ to N_Ω, $\overline{S}_1 = g^{-1} N_\Omega^{-1} \sum_{l=1}^{N_\Omega} \sum_{l'=1}^{N_\Omega} w_{l'} \hat{p}_{ll'} \boldsymbol{\Omega}_l \cdot \boldsymbol{\Omega}_{l'}$ is calculated. u_{th} is updated for $\overline{S}_1$ to reach its theoretical value of unity using the Levenberg-Marquardt method.

Step (v) *Repetition from Step (ii) to Step (iv)*: Steps (ii)-(iv) are repeated until the difference of $|\overline{S}_1 - 1|$ is sufficiently small. After the repetition, u_{th} and $\hat{p}_{ll'}$ are determined.

The reasons of employing the DEF for the determination of $W_{ll'}$ are as follows. The DEF has been originally developed for fast convergence of numerical integration with end point singularities (Takahasi and Mori, 1974; Mori and Sugihara, 2001). For the case of highly forward-peaked scattering, the phase function exponentially increases near the end point of $\boldsymbol{\Omega}_l \cdot \boldsymbol{\Omega}_{l'} = 1$. Also, the weight matrix satisfies the symmetry condition of $W_{ll'} = W_{l'l}$, as clearly seen from Eq. (9).

2.4. Finite difference method

In the finite difference method, x, y, z, and t are discretized as $x_i = i\Delta x$ ($i \in \{0, \cdots, N_x\}$), $y_j = j\Delta y$ ($j \in \{0, \cdots, N_y\}$), $z_k = k\Delta z$ ($k \in \{0, \cdots, N_z\}$), and $t_m = m\Delta t$ ($m \in \{0, \cdots, N_t\}$) with the constant step sizes of Δx, Δy, Δz, and Δt, respectively, and the numbers of the grid nodes and timesteps of N_x, N_y, N_z, and N_t, respectively.

The third order weighted essentially non-oscillatory (WENO) scheme (Jiang and Shu, 1996; Henrick et al., 2005) is employed for spatial discretization in this study. For calculation of the advection term of $\boldsymbol{\Omega} \cdot \nabla I(\boldsymbol{r}, \boldsymbol{\Omega}, t)$ in the RTE, the first order upwind (Klose et al., 2002; Fujii et al., 2014), diamond difference (Klose and Larsen, 2006), and third order upwind (Fujii et al., 2016) schemes have been employed. The diamond difference and third order upwind schemes can improve the accuracy of the numerical solution of the RTE when compared with the first order upwind scheme, but these schemes produce numerical oscillations in the time period just before rapid increase of the light

Table 1. Quadrature sets of $(w_l, \mathbf{\Omega}_l)$ and total number of discrete angular directions, N_Ω

$(w_l, \mathbf{\Omega}_l)$	N_Ω								
LSE (Fiveland, 1991)	48	80	120	168	224	288	360		
EO (Endo and Yamamoto, 2007)	48	80	120	168	224	288			
Lebedev (Lebedev, 1975, 1977)	50	86	110	146	170	194	302	350	434
	590	770	974	1202	1454				

intensity, leading to loss of accuracy. In the field of computational fluid dynamics, high order schemes for calculation of the advection term have been developed and the stability of the developed scheme have been investigated (Kannan, 2012). Among them, the WENO scheme can suppress the numerical oscillation by considering non-linear weights based on the differences in the numerical solutions of the intensities between the neighboring nodes. In the third order WENO scheme, the advection term of $I_{l,i}(t)$ at a spatial grid node of x_i along the x-axis in the l-th discrete angular direction Ω_{lx} is given as follows:

$$\Omega_{lx}\frac{\partial I_{l,i}}{\partial x} \sim \frac{1}{2}\Omega_{lx}\left[v_{2,i} + v_{3,i} - \omega_i(v_{1,i} - 2v_{2,i} + v_{3,i})\right], \tag{10}$$

where $v_{q,i}$ $(q = 1, 2, 3)$ represents discretized gradients of the intensity,

$$\begin{cases} v_{1,i} = (I_{l,i-1} - I_{l,i-2})/\Delta x, & v_{2,i} = (I_{l,i} - I_{l,i-1})/\Delta x, & v_{3,i} = (I_{l,i+1} - I_{l,i})/\Delta x & \Omega_{lx} \geq 0 \\ v_{1,i} = (I_{l,i+2} - I_{l,i+1})/\Delta x, & v_{2,i} = (I_{l,i+1} - I_{l,i})/\Delta x, & v_{3,i} = (I_{l,i} - I_{l,i-1})/\Delta x & \Omega_{lx} < 0. \end{cases} \tag{11}$$

The non-linear weight, ω_i, is given so as to avoid overshoot and undershoot at a discontinuous region,

$$\omega_i = \frac{1}{1 + 2r_s^2}, \qquad r_s = \frac{\epsilon + (v_{2,i} - v_{1,i})^2}{\epsilon + (v_{3,i} - v_{1,i})^2}, \tag{12}$$

where r_s is a ratio of the smooth indicators; and ϵ is a parameter to avoid division by zero and set as 10^{-4} here, while it is set as 10^{-6} in the original paper (Jiang and Shu, 1996). We confirmed that the numerical results of the RTE were insensitive to the choice of ϵ, either 10^{-4} or 10^{-6}.

For temporal discretization, the third order TVD (total variation diminishing)-Runge-Kutta method (Gottlieb and Shu, 1998) is employed. Refer (Fujii et al., 2017) for the details.

At the boundary of a medium, the refractive-index mismatched boundary condition is employed. Refer (Fujii et al., 2014) for the details.

The finite difference method has several advantages; the programming code is easily implemented to improve the accuracy by the high order schemes, the accessibility by parallel computing, and the efficiency by low data storage format compared with the finite element and volume methods. A comparison study for numerical solutions of the RTE using the several methods should be discussed in future.

2.5. Measurement quantities and numerical conditions

This paper considers three kinds of the quadrature sets: LSE (Fiveland, 1991), EO (Endo and Yamamoto, 2007), and Lebedev (Lebedev, 1975, 1977) quadrature sets with various values of N_Ω as listed in Table 1, two kinds of

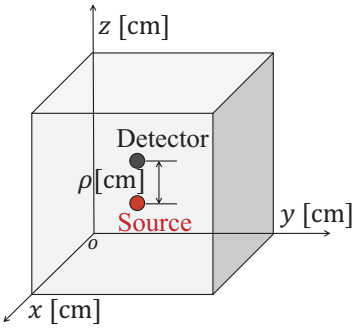

Fig. 3. Source and detector positions in the homogeneous cubic medium

renormalization approaches: conventional approach (Eq. (7)) and developed approach (Eqs. (8) and (9)), and two cases of highly forward-peaked scattering: $g = 0.8$ and 0.9.

2.5.1. L-th order normalization condition

To examine the L-th order normalization condition (Eq. (6)) of the renormalized phase function, we consider numerical integration, S_L^l, defined as

$$S_L^l = g^{-L} \sum_{l'=1}^{N_\Omega} w_{l'} \hat{p}_{ll'} P_L(\mathbf{\Omega}_l \cdot \mathbf{\Omega}_{l'}) \qquad l = 1, 2, \cdots, N_\Omega, \tag{13}$$

which should ideally be unity. We calculated the mean value of S_L^l averaged over the whole range of l, defined as $\overline{S}_L = \sum_{l=1}^{N_\Omega} S_L^l / N_\Omega$, and the mean absolute percentage error of S_L^l, defined as

$$e_L = \sum_{l=1}^{N_\Omega} |S_L^l - 1| \times 100 / N_\Omega. \tag{14}$$

Here, the results of the zeroth order normalization condition (Eq. (6) with $L = 0$) are not shown, but it was confirmed that $\overline{S}_0$ was unity and e_0 was zero for all the quadrature sets, for all the renormalization approaches, and for all the cases of g.

2.5.2. Fluence rate

For examination of the accuracy of the numerical solution of the RTE using the renormalization approaches, we calculated temporal profiles of the fluence rate, $\Phi(\boldsymbol{r}, t) = \int_{4\pi} d\mathbf{\Omega} I(\boldsymbol{r}, \mathbf{\Omega}, t)$ and compared the numerical solution of the RTE with the analytical solution of the RTE for infinite homogeneous media.

Analytical solution of the RTE. Recently, the RTE with anisotropic scattering ($g \neq 0$) has been analytically solved in time domain using a single-sided Laplace transformation of the spherical harmonics expansions (Liemert and Kienle, 2012). The analytical solution of the time-domain fluence rate, $\Phi_{RTE}(r, t)$, for infinite media is given as

$$\Phi_{RTE}(r, t) = \frac{1}{2rR^2} \sum_{\kappa=1}^{\infty} \kappa I_{\kappa 0}(t) \sin(\xi_{\kappa 0} r), \tag{15}$$

where $r = |\boldsymbol{r}|$, R represents the radius of a large sphere, κ discrete wavenumber, $I_{\kappa 0}(t)$ the time-dependent mode of the intensity, $\xi_{\kappa 0}$ the positive root of the equation of $j_0(\xi_{\kappa 0}R) = 0$ with j_0 being the zeroth order spherical Bessel function of the first kind. The analytical solution (Eq. (15)) was verified by comparisons with Monte Carlo simulations and experimental data (Kamran et al., 2015). Because Eq. (15) forms the summation over κ, numerical calculation is partially necessary. Hence, we employed an open source MATLAB code (Liemert and Kienle, 2012) for the numerical calculation of Eq. (15).

Object for calculation. Figure 3 shows a homogeneous cubic medium with a side of 2.2 cm as an object, in which a source was located near the center of the medium $\boldsymbol{r}_s = (x_s, y_s, z_s) = (1.10\text{ cm}, 1.10\text{ cm}, 0.88\text{ cm})$, and a detector at $\boldsymbol{r}_d = (x_s, y_s, z_s + \rho)$ with a source-detector distance of $\rho = |\boldsymbol{r}_s - \boldsymbol{r}_d|$. The reason why the source and detector were located inside the medium is for comparison of the analytical solutions of the RTE in infinite media with the numerical solutions of the RTE in finite media by suppressing the boundary effects. Our preliminary studies (unpublished data) showed that numerical results of Φ were little influenced in the time period of interest by changing the boundary conditions from the refractive-index mismatching to the non-reentry boundary conditions, and by increasing the medium size. These results confirmed the verification of comparing the analytical solutions in the infinite media with the numerical solutions in the finite media under the conditions employed in this study.

Although data are not shown, the invariances of the numerical solutions with respect to 90-degree axis rotation and line reflection were examined by comparing with the numerical solutions at six detector positions: $(x_s \pm \rho, y_s, z_s)$, $(x_s, y_s \pm \rho, z_s)$, and $(x_s, y_s, z_s \pm \rho)$ when ρ was fixed. It was shown that the numerical solutions with the LSE, EO, and Lebedev sets satisfied the invariances; they were the same for all the six detector positions with each quadrature set. Hence, in this paper, only the numerical solutions detected at $(x_s, y_s, z_s + \rho)$ are shown.

Evaluation of the numerical results. In this paper, we investigate the shape difference in the temporal profiles of the fluence rate normalized by their peak values, $\hat{\Phi}$, between the numerical and analytical solutions of the RTE, without discussion of their magnitudes. This is because the normalized profiles are less sensitive to the differences in the conditions between the numerical and analytical solutions; for example, the numerical scheme considers the source profile as a pulse function, while the analytical scheme as a delta function. The difference in $\hat{\Phi}$ between the numerical and analytical solutions of the RTE was evaluated by the mean absolute percentage error, e_Φ

$$e_\Phi = \frac{1}{M_2 - M_1} \sum_{m=M_1}^{M_2} \left| \frac{\hat{\Phi}^m - \hat{\Phi}_{RTE}(t_m)}{\hat{\Phi}_{RTE}(t_m)} \right| \times 100, \tag{16}$$

where $\hat{\Phi}^m$ and $\hat{\Phi}_{RTE}(t_m)$ represent the numerical and analytical solutions for $\hat{\Phi}$ at the m-th time step, t_m, respectively; and the summation with respect to m is over the time period from the time of t_{M_1} when $\hat{\Phi}_{RTE}$ reaches $10^{-0.5} \backsimeq 0.316$ before the peak to the time of t_{M_2} when $\hat{\Phi}_{RTE}$ falls to $10^{-1.5} \backsimeq 0.032$ after the peak. Here, a time period earlier than t_{M_1} is excluded from the calculation of e_Φ because the analytical solution (Eq. (15)) oscillates in the early time period due to the spherical harmonics expansion, and because in the numerical solution the rise of the temporal profile from zero is less sharp than in the analytical solution.

Table 2. Optical properties of the numerical phantoms and source-detector distance, ρ

	μ_a[cm^{-1}]	μ_s[cm^{-1}]	g	n	ρ [cm]
Phantom 1 (Klose et al., 2002)	0.35	58.0	0.8	1.56	0.36
Phantom 2 (Bashkatov et al., 2011)	0.3	80.0	0.9	1.4	0.46

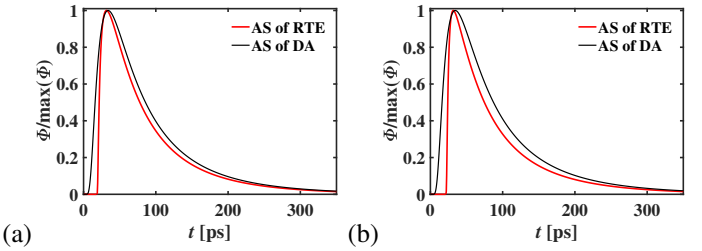

Fig. 4. Analytical solutions (AS) of the RTE (Eq. (15)) and the DA (Chandrasekhar, 1943) with the diffusion coefficient $D = [3\mu_s(1-g)]^{-1}$ for the infinite media: (a) Phantom 1 at $\rho = 0.36$ cm and (b) Phantom 2 at $\rho = 0.46$ cm, as listed in Table 2.

2.5.3. Optical properties and computation loads

Two examples of numerical phantoms are considered: Phantom 1 with the optical properties of a mixture of SiO_2 particles and ink embedded in epoxy resin (Klose et al., 2002), and Phantom 2 with the optical properties of background tissue of the human neck averaged over the muscle, adipose tissue, and bone (Bashkatov et al., 2011). The optical properties of the two numerical phantoms are listed in Table 2. ρ were given as 0.36 cm and 0.46 cm for Phantoms 1 and 2, respectively. Figures 4(a) and (b) show that the analytical solutions of the RTE and the DA (Chandrasekhar, 1943) for the infinite media with the conditions as listed in Table 2, where the diffusion coefficient D is given as $[3\mu_s(1-g)]^{-1}$ (Furutsu and Yamada, 1994). It is observed that the DA leads to large deviations from the RTE.

The spatial and temporal step sizes were determined as $\Delta x = \Delta y = \Delta z = 0.02$ cm and $\Delta t = 0.5$ ps, respectively by preliminary investigation of the numerical solutions of the RTE with different values of the step sizes. The preliminary investigation showed that Φ was unchanged even as the step sizes were finer than those given above.

The source code for the numerical calculation was written in the C programming language, and all the matrices were compressed to vectors as the compressed row storage format. Also, parallel CPU programming was implemented with 48 thread computers (Intel Xeon E5-2690v3@ 2GHz) by using the OpenMP, which is a portable and shared-memory programming scheme.

Table 3 lists the matrix size ($N_xN_yN_zN_\Omega \times N_xN_yN_zN_\Omega$) and computation time for calculation of Φ in the time period of [0 ps, 350 ps] with the LSE set using the conventional renormalization approach (Eq. (7)) for Phantom 1. The ratios of the matrix sizes and computation times for the cases with $N_\Omega < 360$ to those with $N_\Omega = 360$ are also listed in Table 3. It should be noted that in our calculations, the computation times using the EO set and the developed approach are almost the same as those listed in Table 3 when N_Ω is the same, because the developed approach requires additional computation time of only a few seconds over the conventional approach. Also, the computation times are independent of the kinds of the numerical phantoms because the spatial and temporal sizes are fixed; the numbers of spatial grid nodes ($N_xN_yN_z$) and timesteps N_t are 1030301 and 700, respectively.

Table 3. Memory requirements and CPU times for the LSE set

	N_Ω						
	48	80	120	168	224	288	360
Matrix size [$\times 10^{17}$]	0.025	0.068	0.153	0.300	0.533	0.881	1.376
Ratio of Matrix size	0.018	0.049	0.111	0.218	0.387	0.640	1.000
CPU time [hour]	3.33	5.44	6.29	10.30	18.24	29.37	34.93
Ratio of CPU time	0.095	0.156	0.180	0.295	0.522	0.841	1.000

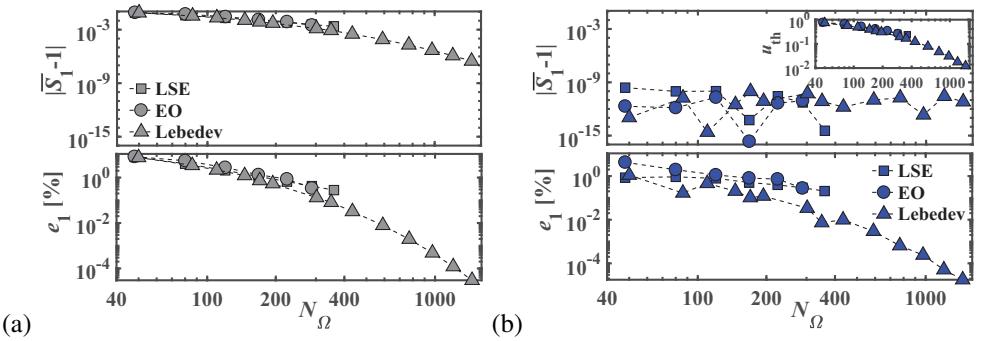

Fig. 5. Evaluation of numerical integral of the first order normalization condition, S_1^l, for the three kinds of quadrature sets listed in Table 1 in the case of $g = 0.8$ using (a) the conventional zeroth order renormalization approach (Eq. (7)) and (b) the developed first order renormalization approach (Eqs. (8) and (9)). (Top row) mean values errors of S_1^l, $|\overline{S}_1 - 1|$ and (bottom row) mean absolute percentage errors of S_1^l, e_1, as a function of N_Ω in the double-logarithmic scales. u_{th} is plotted in the inset of the top row of the figure (b).

3. Numerical results

3.1. The case of $g = 0.8$

3.1.1. L-th order normalization condition

Firstly, we examine the first order normalization condition of the renormalized phase function (Eq. (6) with $L = 1$) for the three quadrature sets listed in Table 1 in the case of $g = 0.8$. Figure 5(a) shows the results of $|\overline{S}_1 - 1|$ and e_1 using the conventional zeroth order renormalization approach (Eq. (7)). It is observed that as N_Ω increases, $|\overline{S}_1 - 1|$ and e_1 approach to zero for all the quadrature sets. Also, it is observed that the convergences of $|\overline{S}_1 - 1|$ and e_1 for the three sets are similar to each other while the accuracies of the quadrature sets are different from each other. The

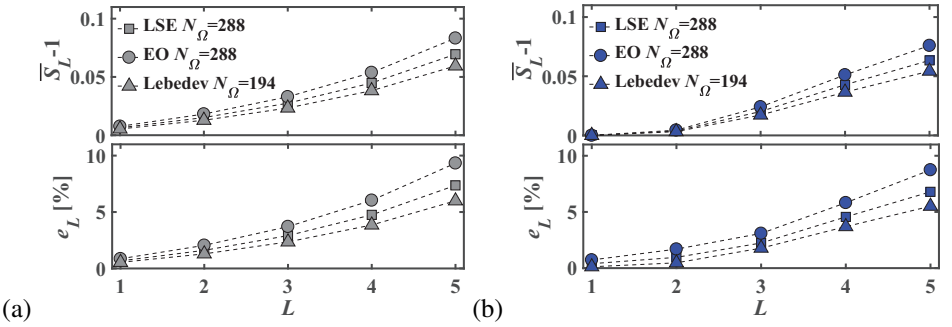

Fig. 6. Evaluation of numerical integral of the L-th order normalization condition, S_L^l, for the LSE set ($N_\Omega = 288$), EO set ($N_\Omega = 288$), and Lebedev set ($N_\Omega = 194$) using (a) the conventional renormalization approach and (b) the developed renormalization approach. (Top row) mean value errors of S_L^l, $\overline{S}_L - 1$ and (bottom row) mean absolute percentage errors of S_L^l, e_L.

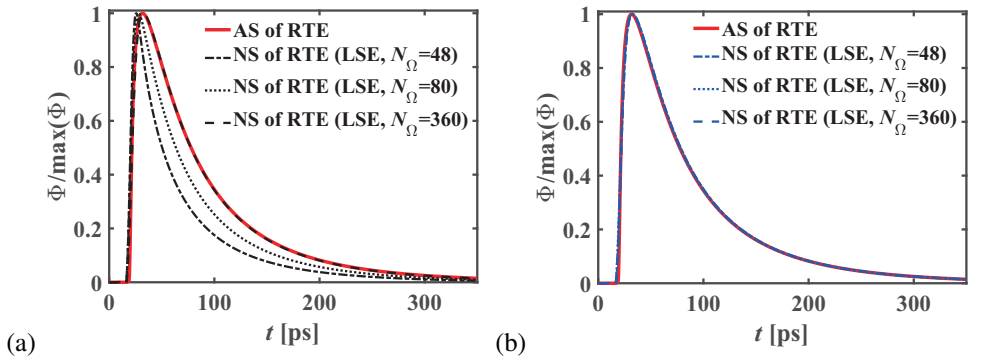

Fig. 7. Temporal profiles of the fluence rate, Φ, normalized by their peak values in the case of Phantom 1 ($g = 0.8$) as listed at Table 2 using (a) the conventional renormalization approach and (b) developed renormalization approach. The numerical solutions (NS) of the RTE for the LSE set with different values of $N_\Omega = 48$, 80 and 360; and the analytical solutions (AS) of the RTE (Eq. (15)).

similar behavior comes from the introduction of the renormalizing factor, f_l, in Eq. (7).

Figure 5(b) shows the results using the first order renormalization approach, developed here as Eqs. (8) and (9). The results of $|\overline{S}_1 - 1|$ take values less than 10^{-9} over all the values of N_Ω and over all the sets by adjusting u_{th} so as to satisfy the first order normalization condition. The adjusted values of u_{th} with the three sets are shown in the inset of Fig. 5(b) (top row), indicating that u_{th} is less dependent on the kinds of the sets. The inset also shows that u_{th} decreases as N_Ω increases, meaning less contributions of the developed approach to the convergence because the weight matrix, $W_{ll'}$, is constant for $|u_{ll'}| > u_{th}$ as in Eq. (9). As shown in the bottom row of Fig. 5(b), the developed approach can reduce the errors, e_1, for $N_\Omega \lesssim 300$ when compared with the conventional approach, while for $N_\Omega \gtrsim 300$ the errors using the developed approach are almost the same as those using the conventional approach. These results for $N_\Omega \gtrsim 300$ comes from the fact that $\hat{p}_{ll'}$ calculated using the developed approach is almost the same as that using the conventional approach due to constant values of $W_{ll'}$ over all the values of $u_{ll'}$. The bottom row of Fig. 5(b) also shows that the results of e_1 using the developed approach depend on the kinds of quadrature sets, compared with those using the conventional approach. This is because the values of $W_{ll'}$ depend on the values of $\mathbf{\Omega} \cdot \mathbf{\Omega}'$ unlike f_l. Among the three quadrature sets, the LSE and Lebedev sets can efficiently reduce the errors within 1% over all the values of N_Ω.

It is observed in Figs. 5(a) and (b) that for $N_\Omega \gtrsim 200$, $|\overline{S}_1 - 1|$ and e_1 take values less than 10^{-2} and 1, respectively for the three quadrature sets and two renormalization approaches. Then, it is interesting to investigate whether the higher order normalization conditions (Eq. (6) with $L > 1$) can be satisfied for $N_\Omega \gtrsim 200$. Figures 6(a) and (b) show $\overline{S}_L - 1$ and e_L calculated with different values of L using the LSE set ($N_\Omega = 288$), EO set ($N_\Omega = 288$), and Lebedev set ($N_\Omega = 194$). As the order of normalization, L, increases, $\overline{S}_L - 1$ and e_L increase for both of the conventional and developed renormalization approaches, although the developed approach can slightly reduce the errors for large L. In future, a new renormalization approach should be developed to satisfy the higher order normalization conditions with $L > 1$.

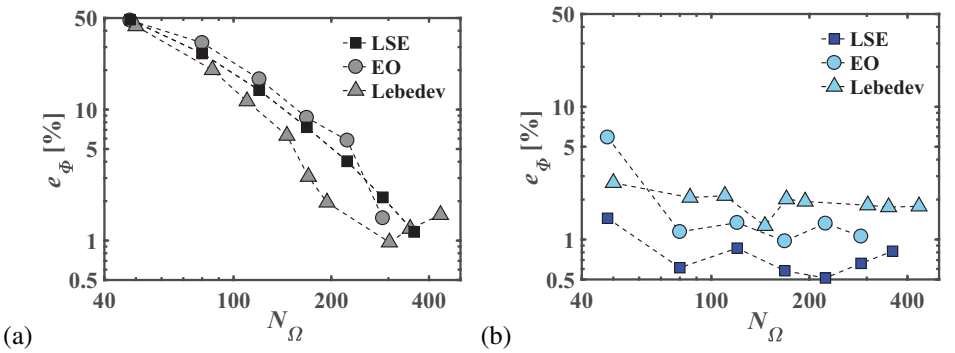

Fig. 8. The difference in Φ, e_Φ, between the numerical and analytical solutions of the RTE with different values of N_Ω for the three quadrature sets using (a) the conventional and (b) developed renormalization approaches in Phantom 1 ($g = 0.8$) at the double-logarithmic scales.

3.1.2. Fluence rate

In this subsection, we examine the numerical solutions of the RTE in Phantom 1 ($g = 0.8$) as listed at Table 2 for the three quadrature sets with different values of N_Ω using the two renormalization approaches.

Figure 7(a) shows the temporal profiles of Φ obtained by numerical solutions using the conventional approach for the LSE set with three values of $N_\Omega = 48$, 80, and 360; and by the analytical solution (Eq. (15)). As shown in Fig. 7(a), the numerical solutions are strongly influenced by the values of N_Ω even though the spatial and temporal step sizes are the same. The numerical solution with $N_\Omega = 360$ agrees well with the analytical solution while the numerical solutions with $N_\Omega = 48$ and 80 significantly deviate from the analytical solution. These deviations are attributed to the numerical errors of the normalization conditions of the phase function and of the scattering integral (Eq. (4)).

Figure 7(b) shows the numerical solutions of the RTE using the developed approach under the same conditions as the case of the conventional approach. In contrast to the results using the conventional approach, all the solutions agree very well with the analytical solution. The results verify that the developed approach can improve the accuracy of the numerical solutions for highly forward-peaked scattering.

Figure 8 shows the difference in Φ, e_Φ (Eq. (16)), between the numerical and analytical solutions for the three quadrature sets with different values of N_Ω using the two renormalization approaches. As shown in Fig. 8(b), the developed approach can reduce the errors within 6 % with all the values of N_Ω. The results of e_Φ are quite similar to those of e_1 as shown in Fig. 5(b) (bottom row) with the exception of largest values of e_Φ for the Lebedev set while smallest values of e_1 for the Lebedev set among the three quadrature sets in the domain of N_Ω larger than 48. Comparisons of e_1 and e_Φ, especially focused on the results for the LSE set, show that e_1 needs to be reduced to less than 1 % to attain the accurate numerical solutions with e_Φ less than 2%. The requirement to e_1 seems very hard, but this comes probably from the fact that e_L ($L > 1$) for the higher order normalization condition is still large even at the small values of e_1. In addition, it is suggested that the positive correlation between e_1 and e_Φ enables efficient evaluations of the accuracy of the numerical solution without calculations of the RTE.

From the above results, the LSE set with $N_\Omega = 48$ using the developed approach is the best choice for the accuracy

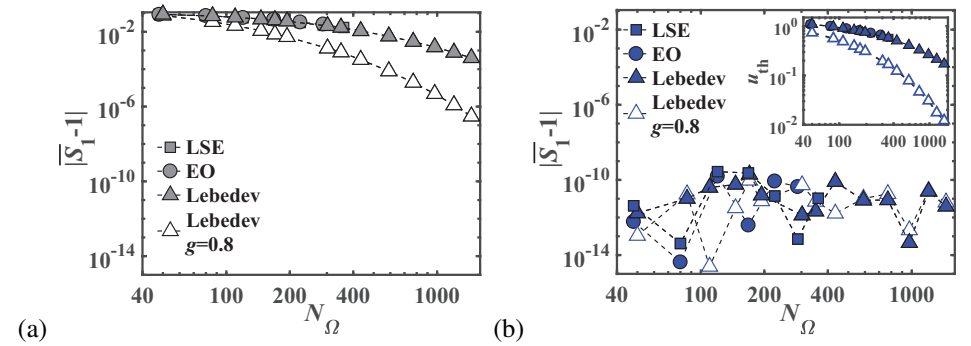

Fig. 9. Results of $|\overline{S}_1 - 1|$ in the case of $g = 0.9$ using (a) the conventional renormalization approach and (b) developed renormalization approach. As a reference, the results for the Lebedev set in the case of $g = 0.8$ are plotted by open triangles. Other details are the same as in Fig. 5.

and efficiency among the three quadrature sets because of the small errors of the numerical results and of the lowest computation loads. When we compare the case for the LSE set with $N_\Omega = 360$ using the conventional approach with the case for the LSE set with $N_\Omega = 48$ using the developed approach, the values of e_Φ for both cases are almost the same less than 2 % as shown in Fig. 8, while as listed in Table 3, CPU time in the case of the developed approach is approximately ten times lower than that in the case of the conventional approach.

3.2. The case of $g = 0.9$

3.2.1. L-th order normalization condition

In this subsection, we examine the first order normalization condition in the case of $g = 0.9$ for the three quadrature sets as listed at Table 1 with different values of N_Ω using the conventional and developed renormalization approaches.

The results of $|\overline{S}_1 - 1|$ using the conventional approach are plotted in Fig. 9(a) showing the slower convergence of $\overline{S}_1$ to unity with N_Ω than those in the case of $g = 0.8$ (open triangles). To achieve the convergence, hence, the maximum values of $N_\Omega = 360$ and 288 for the LSE and EO sets are insufficient, and a larger value of N_Ω for the Lebedev set is required. Although data not shown here, the values of $|\overline{S}_L - 1|$ with $L > 1$ in the case of $g = 0.9$ are also larger than those in the case of $g = 0.8$. These results come from the steeper change of the phase function toward $\mathbf{\Omega} \cdot \mathbf{\Omega}' = 1$ in the case of $g = 0.9$ than in the case of $g = 0.8$ as shown in Fig. 2. Figure 9(b) shows the results of $|\overline{S}_1 - 1|$ using the developed approach and the adjusted values of u_{th} (inset). Similarly to the results in the case of $g = 0.8$ (open triangles), it is observed that $|\overline{S}_1 - 1|$ take values less than 10^{-9} with all the values of N_Ω, and u_{th} decreases as N_Ω increases. Also, u_{th} in the case of $g = 0.9$ is larger than that in the case of $g = 0.8$ with the fixed values of N_Ω, meaning that the phase function with $g = 0.9$ is renormalized in a wider range of $\mathbf{\Omega}_l \cdot \mathbf{\Omega}_{l'}$ than that with $g = 0.8$.

In Figs. 10(a) and (b), the results of e_1 using the two renormalization approaches are compared. Similarly to the results in the case of $g = 0.8$ (bottom row of Figs. 5(a) and (b)), the developed approach can reduce the errors compared to the conventional approach especially with the small values of N_Ω. As shown in Fig. 10(b), e_1 take values less than 1 % for the LSE set with $N_\Omega = 48$ and for the Lebedev set in the domain of $N_\Omega \gtrsim 80$. Also, the results using the LSE set behave differently from those using the EO and Lebedev sets; e_1 using the LSE set increases as N_Ω increases from 48 to 120 while e_1 using the EO and Lebedev sets tend to decrease. The reason of the behavior for the

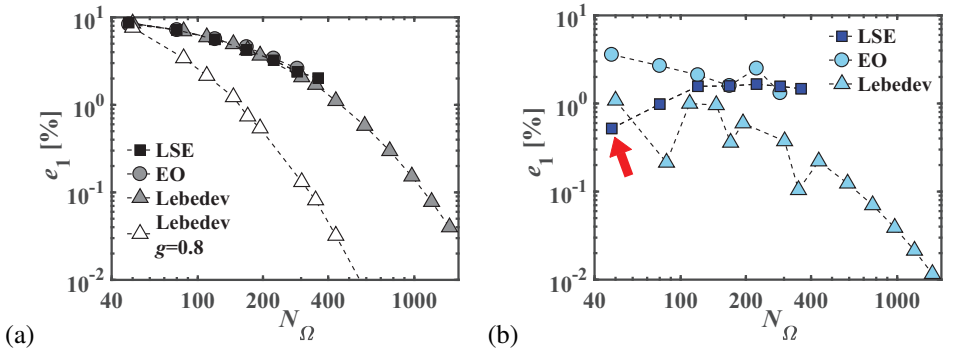

Fig. 10. Results of e_1 in the case of $g = 0.9$ using (a) the conventional and (b) developed renormalization approaches. Other details are the same as in Fig. 9.

LSE set is discussed in the following. Because the developed approach determines the values of $W_{ll'}$ as a function of $\mathbf{\Omega}_l \cdot \mathbf{\Omega}_{l'}$, the distribution of $\mathbf{\Omega}_l$, especially its uniformity, affects the results of e_1; the better uniformity tends to smaller values of e_1. This tendency is enhanced in the case of $g = 0.9$ compared with the case of $g = 0.8$. Although data are not shown, for the LSE set with $N_\Omega = 48$, the $\mathbf{\Omega}_l$-distribution is completely uniform but with $N_\Omega = 80$ and 120, the uniformity becomes worse. These behaviors of the $\mathbf{\Omega}_l$-distribution for the LSE set probably contribute to the increase of e_1 with the increase of N_Ω.

From Fig. 10(b), it is suggested that the LSE set with $N_\Omega = 48$ (denoted by the red arrow) can provide more accurate numerical solution of the RTE with lower computation loads among the three quadrature sets over the whole domain of N_Ω. The suggestion for the accuracy comes from the fact that e_1 is correlated with e_Φ as discussed in the above, and the suggestion for the efficiency comes from the fact that N_Ω is directly related to computation loads as shown in Table 3. This suggestion will be verified in the next subsection by examining the accuracy of the numerical solutions of the RTE.

3.2.2. Fluence rate

Figure 11(a) shows the normalized temporal profiles of the fluence rate, $\hat{\Phi}$, numerically calculated from the RTE using the two renormalization approaches for Phantom 2 ($g = 0.9$) and compares them with the analytical solution of the RTE (Eq. (15)). Here, the LSE set with $N_\Omega = 48$ is chosen as stated above. As shown in Fig. 11(a), the numerical solution using the developed approach agrees well with the analytical solution, while the numerical solution using the conventional approach significantly deviates from the analytical solution. The result verifies the suggestion discussed in the previous subsection. In Fig. 11(b), the errors, e_Φ, using the conventional (gray marks) and developed (blue marks) approaches are shown as a function of N_Ω for Phantom 2. The developed approach can reduce the errors especially with the smaller values of N_Ω; in the range of $N_\Omega \lesssim 100$, e_Φ for the developed approach decreases by one-fourth of that for the conventional approach. From Fig. 11(b), it is found that over the whole domain of N_Ω except 48 and 302, the Lebedev set can provide the most accurate solutions of the RTE among the three quadrature sets in the case of $g = 0.9$.

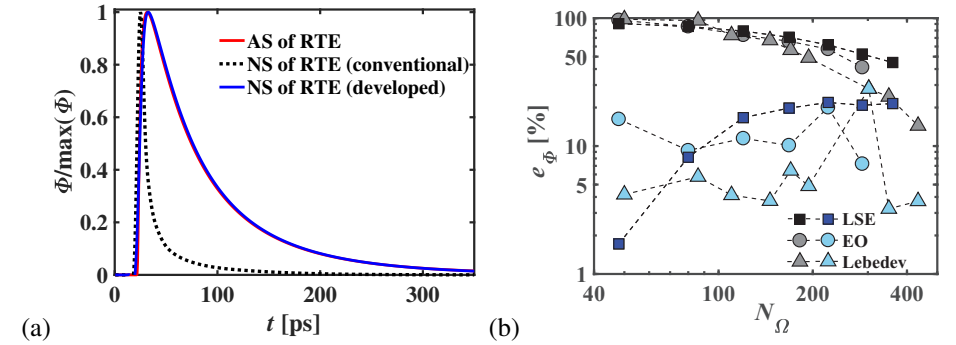

Fig. 11. (a) Temporal profiles of Φ for numerical calculation for the LSE set with $N_\Omega = 48$ using the two renormalization approaches in Phantom 2 ($g = 0.9$) listed at Table 2. Other details are the same as Fig. 7. (b) The errors, e_Φ, using the conventional (gray marks) and developed (blue marks) approaches in Phantom 2. Other details are the same as in Fig. 8.

Table 4. The numerical results for $e_1[\%]$ and $e_\Phi[\%]$ using the Galerkin quadrature method and developed renormalization approach at the LSE set with $N_\Omega = 48$.

	$e_1[\%]$		$e_\Phi[\%]$	
	$g = 0.8$	$g = 0.9$	$g = 0.8$	$g = 0.9$
Galerkin quadrature method (Morel, 1989)	0.36×10^{-15}	0.36×10^{-15}	1.69	2.19
Developed renormalization approach	0.85	0.52	1.45	1.72

3.3. Comparison with the Galerkin quadrature method

We test the accuracy and efficiency of the developed renormalization approach by comparing with the Galerkin quadrature method or the Galerkin approach for brevity. The Galerkin approach has been developed to treat highly forward-peaked scattering of charged particles, and can provide the accurate and efficient numerical results (Morel, 1989; Morel et al., 2017). As a quadrature set, here, the LSE set with $N_\Omega = 48$ is chosen for both approaches because the set is best for accurate and efficient solutions of the RTE using the developed approach. The formulation of the Galerkin approach is outlined in Appendix.

The numerical results of e_1 (Eq. (14) for $L = 1$) using the Galerkin and the developed approaches are listed in Table 4 for the cases of $g = 0.8$ and 0.9. In the Galerkin approach, Eq. (13) for $L = 1$ is modified to $g^{-1} \sum_{l'=1}^{N_\Omega} p_{G,ll'} P_1(\boldsymbol{\Omega}_l \cdot \boldsymbol{\Omega}_{l'})$ without using the weight, $w_{l'}$, but with using the phase function matrix, $\boldsymbol{p}_G$. Compared with the developed approach, the Galerkin approach can reduce the errors remarkably for both cases of the g-values, suggesting the accuracy and efficiency of the Galerkin approach for calculations of the scattering integral in highly forward-peaked scattering. This superiority of the Galerkin approach is attributed to the fact that the Galerkin approach uses the orthogonality of the spherical harmonics, while the developed approach does not.

Figure 12 plots the numerical solutions of the RTE using the Galerkin and the developed approaches, and the analytical solutions (Eq. (15)), showing very good agreements between them for both cases of (a) $g = 0.8$ and (b) 0.9. The numerical results of e_Φ (Eq. (16)) using the Galerkin and the developed approaches are listed in Table 4. It shows that the errors using the Galerkin approach are similar to those using the developed approach, although the values of e_1 are quite different from each other. These results suggest that the values of e_1 less than 1% are sufficient to obtain accurate solutions of the RTE.

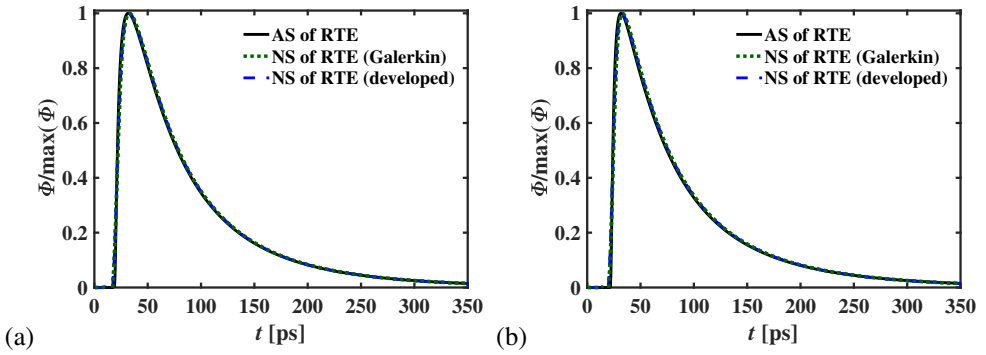

Fig. 12. Numerical results of the fluence rate, Φ, normalized by their peak values using the Galerkin and the developed approaches at the LSE set with $N_\Omega = 48$ for (a) $g = 0.8$ and (b) 0.9. Other details are the same as in Fig. 11(a).

The required memory and computation times for solving the RTE using the Galerkin approach are almost the same as those using the developed approach, which are listed in Table 3 for the case of $N_\Omega = 48$ because the computation time to generate $\boldsymbol{p}_G$ is few seconds.

From these results, it is suggested that the developed approach can provide almost the same accuracy and efficiency of the numerical solutions of the RTE as the Galerkin approach.

4. Conclusions

We have developed the first order renormalization approaches of the highly forward-peaked phase function in the RTE using the DEF for the three quadrature sets. We have compared the numerical solutions of the RTE using the developed renormalization approach with those using the conventional zeroth order renormalization approach. The comparative studies show that the developed approach can successfully reduce the numerical errors than the conventional approach.

Among the three quadrature sets, the LSE set can provide more accurate results of e_1 and e_Φ over the whole domain of N_Ω in the case of $g = 0.8$, meanwhile the Lebedev set can in the case of $g = 0.9$. When we can choose smaller values of N_Ω, the LSE set with $N_\Omega = 48$ using the developed approach is found to be the best choice for accurate and efficient calculation of the RTE (calculation of the fluence rate) in both cases of $g = 0.8$ and 0.9.

We have compared numerical results using the developed approach with those using the Galerkin approach, which formulates the scattering integral in a different way from the renormalization approach, for the recommended set, the LSE set with $N_\Omega = 48$. It is found that the results of e_Φ using both approaches are almost the same although the results of e_1 using the Galerkin approach are remarkably less than those using the developed approach.

Appendix A. Outline of the Galerkin quadrature method

We outline the formulation of the Galerkin quadrature method or Galerkin approach for brevity in a 3D geometry. For the details of the method, refer the original papers (Morel, 1989; Morel et al., 2017). In the Galerkin approach, it is required that the residual of the scattering integral is orthogonal to the weighting space, where the spherical

harmonics form basis functions for 3D case. Based on the Galerkin approach, the matrix of the phase function $\boldsymbol{p}_G$ at a given spatial grid point is formulated as

$$\boldsymbol{p}_G = \boldsymbol{M}\boldsymbol{\Sigma}\boldsymbol{D}, \tag{A.1}$$

where $\boldsymbol{M}$ is the moment-to-direction matrix, $\boldsymbol{\Sigma}$ the cross section matrix, and $\boldsymbol{D}$ the direction-to-moment matrix, respectively. In the Galerkin approach, the relation of $\boldsymbol{M}\boldsymbol{D} = \boldsymbol{I}$ holds, where $\boldsymbol{I}$ is the unit matrix. Each element of the moment-to-direction matrix, M_{ld}, is calculated using the tesseral or real spherical harmonics of degree n and order m, Y_n^m;

$$M_{ld} = Y_n^m(\boldsymbol{\Omega}_l), \qquad l = 1, 2, \cdots, N_\Omega, \qquad d = 0, 1, \cdots, N_\Omega - 1, \tag{A.2}$$

where $\boldsymbol{\Omega}_l$ denotes the l-th discrete angular direction; and d corresponds to a combination of indices of n and m, sorted in an arbitrary numbering order, *e.g.*, $d = 0$ for $(n, m) = (0, 0)$, $d = 1$ for $(n, m) = (1, -1)$, and so on. It is noted that the Galerkin approach does not use the weight, w_l, of the quadrature set for computation of $\boldsymbol{p}_G$. The number of the discrete angular direction, N_Ω, is related to the maximum degree of Y_n^m, N_n, as $N_\Omega = N_n(N_n + 2)$ in the LSE set, *e.g.*, $N_\Omega = 48$ for $N_n = 6$. $Y_n^m(\boldsymbol{\Omega}_l)$ is defined as

$$Y_n^m(\boldsymbol{\Omega}_l) = \begin{cases} \sqrt{(2 - \delta_{m0})\frac{2n+1}{4\pi}\frac{(n-|m|)!}{(n+|m|)!}}P_n^{|m|}(\cos\theta_l)\cos(m\phi_l) & m \geq 0 \\ \sqrt{\frac{2n+1}{2\pi}\frac{(n-|m|)!}{(n+|m|)!}}P_n^{|m|}(\cos\theta_l)\sin(|m|\phi_l) & m < 0 \end{cases}, \tag{A.3}$$

where $\boldsymbol{\Omega}_l$ is represented by (θ_l, ϕ_l) in a spherical coordinate. The number of the spherical harmonics of the degree $N_n - 1$ or less is N_n^2 with $-n \leq m \leq n$, while N_Ω is $N_n(N_n + 2)$, meaning that the number of the spherical harmonics, N_n^2, is smaller than the number of the discrete angular directions, N_Ω. Then, the spherical harmonics of degrees higher than $N_n - 1$ are needed. The interpolation space spanned by Y_n^m with the higher degrees is given as

$$Y_n^m : \begin{cases} -n \leq m \leq n & 0 \leq n \leq N_n - 1 \\ -n \leq m < 0 \text{ and } 0 < m \text{ odd } \leq n & n = N_n \\ -n \leq m \text{ even} < 0 & n = N_n + 1 \end{cases}. \tag{A.4}$$

The cross section matrix $\boldsymbol{\Sigma}$ is given by the coefficients of the Legendre polynomial expansion. In the case of Henyey-Greenstein phase function (Eq. (5)), $\boldsymbol{\Sigma}$ is calculated as

$$\boldsymbol{\Sigma} = \mathrm{diag}\left(g^{n(0)}, g^{n(1)}, \cdots, g^{n(d)}, \cdots, g^{n(N_\Omega - 1)}\right), \tag{A.5}$$

where $n(d)$ represents the degree of Y_n^m and is determined by the index d regardless of the order m, *e.g.*, $n = 0$ for $(d, m) = (0, 0)$, $n = 1$ for $(d, m) = (1, -1)$, and so on.

In this paper, the direction-to-moment matrix $\boldsymbol{D}$ is calculated by inversion of $\boldsymbol{M}$ using the LU decomposition. Using the matrix $\boldsymbol{p}_G$, the phase function matrix for the system is calculated as a block diagonal matrix. For computation

of the RTE using the Galerkin approach, we employ the same numerical schemes as those developed in this paper except generating the phase function.

Acknowledgments

This work was partially supported by JSPS KAKENHI Grant Numbers 15K17980, 15K06125, and 16H02155; and by Japan Agency for Medical Research and Development. The authors would like to thank Drs. S. Okawa, M. Machida, K. Hashimoto, and E. Okada for fruitful discussion.

References

M. Case, Kenneth, F. Zweifel, P, Linear transport theory, Reading, Mass. : Addison-Wesley, 1967.
A. P. Gibson, J. C. Hebden, S. R. Arridge, Recent advances in diffuse optical imaging, Phys. Med. Biol. 50 (2005) R1–R43.
Y. Yamada, S. Okawa, Diffuse Optical Tomography : Present Status and Its Future, Opt. Rev. 21 (2014) 185–205.
A. Kannan, R. and Przekwas, A computational model to detect and quantify a primary blast lung injury using near-infrared optical tomography, Int. J. Numer. Meth. Biomed. Engng. 27 (2011) 13–28.
R. Kannan, A. Przekwas, A near-infrared spectroscopy computational model for cerebral hemodynamics, Int. J. Numer. Meth. Biomed. Engng. 28 (2012) 1093–1106.
V. A. Markel, Modified spherical harmonics method for solving the radiative transport equation, Waves Random Media 14 (2004) L13–L19.
M. Machida, G. Y. Panasyuk, J. C. Schotland, V. A. Markel, The Green's function for the radiative transport equation in the slab geometry, J. Phys. A: Math. Theor. 43 (2010) 065402.
A. Liemert, A. Kienle, Infinite space Green's function of the time-dependent radiative transfer equation, Biomed. Opt. Express 3 (2012) 543.
S. Chandrasekhar, Radiative Transfer, Dover, New York, 1960.
B. G. Carlson, C. E. Lee, Mechanical Quadrature and the Transport Equation, Los Alamos Scientific Laboratory Report 2573 (1961).
D. L. Hardy, Y. Favennec, B. Rousseau, F. Hecht, Specular reflection treatment for the 3D radiative transfer equation solved with the discrete ordinates method, J. Comput. Phys. 334 (2017) 541–572.
W. F. Cheong, S. A. Prahl, A. J. Welch, A review of the optical properties of biological tissue, IEEE J. Quantum Electron 26 (1990) 2166–2185.
J. E. Morel, A Hybrid Collocation-Galerkin-Sn Method for Solving the Boltzmann Transport Equation, Nucl. Sci. Eng. 101 (1989) 72–87.
J. E. Morel, J. S. Warsa, B. C. Franke, A. K. Prinja, Comparison of Two Galerkin Quadrature Methods, Nucl. Sci. Eng. 185 (2017) 325–334.
M. Landesman, J. E. Morel, Angular Fokker-Planck Decomposition and Representation Techniques, Nucl. Sci. Eng. 103 (1989) 1–11.
W. J. Wiscombe, On initialization, error and flux conservation in the doubling method, J. Quant. Spectrosc. Radiat. Transfer 16 (1976) 637–658.
L. Liu, L. Ruan, H. Tan, On the discrete ordinates method for radiative heat transfer in anisotropically scattering media, Int. J. Heat Mass Transfer 45 (2002) 3259–3262.
P. Boulet, A. Collin, J. L. Consalvi, On the finite volume method and the discrete ordinates method regarding radiative heat transfer in acute forward anisotropic scattering media, J. Quant. Spectrosc. Radiat. Transfer 104 (2007) 460–473.
B. Hunter, Z. Guo, Conservation of asymmetry factor in phase function discretization for radiative transfer analysis in anisotropic scattering media, Int. J. Heat Mass Transfer 55 (2012) 1544–1552.
H. Fujii, S. Okawa, Y. Yamada, Y. Hoshi, M. Watanabe, Renormalization of the highly forward-peaked phase function using the double exponential formula for radiative transfer, J. Math. Chem. 54 (2016) 2048–2061.
L. G. Henyey, L. J. Greenstein, Diffuse radiation in the galaxy, J. Astrophys. 93 (1941) 70–83.
W. A. Fiveland, The selection of discrete ordinate quadrature sets for anisotropic scattering, ASME, HTD-vol. 160, Fundamentals of radiation heat transfer (1991) 89–96.
B. G. Carlson, Quadrature Tables of Equal Weight EQn Over the Unit sphere, Los Alamos Scientific Laboratory Report 4734 (1971).
D. Balsara, Fast and accurate discrete ordinates methods for multidimensional radiative transfer. Part I , basic methods, J. Quant. Spectrosc. Radiat. Transfer 69 (2001) 671–707.
T. Endo, A. Yamamoto, Development of New Solid Angle Quadrature Sets to Satisfy Even- and Odd-Moment Conditions, J. Nucl. Sci. Technol. 44 (2007) 1249–1258.
B. A. Gregersen, D. M. York, High-order discretization schemes for biochemical applications of boundary element solvation and variational electrostatic projection methods, J. Chem. Phys. 122 (2005) 194110.
R. Sanchez, Prospects in deterministic three-dimensional whole-core transport calculations, Nucl. Eng. Technol. 44 (2012) 113–150.
F. Long, F. Li, X. Intes, S. P. Kotha, Radiative transfer equation modeling by streamline diffusion modified continuous Galerkin method, J. Biomed. Opt. 21 (2016) 036003.
V. I. Lebedev, Values of the nodes and weights of ninth to seventeenth order gauss-markov quadrature formulae invariant under the octahedron group with inversion, USSR Comput. Math. Math. Phys. 15 (1975) 44–51.
V. I. Lebedev, Spherical quadrature formulas exact to orders 25-29, Siberian Math. J. 18 (1977) 99–107.
H. Takahasi, M. Mori, Double exponential formulas for numerical indefinite integration, Publ. RIMS Kyoto Univ. 9 (1974) 721–741.
M. Mori, M. Sugihara, The double-exponential transformation in numerical analysis, J. Comput. Appl. Math. 127 (2001) 287–296.
G.-S. Jiang, C.-W. Shu, Efficient Implementation of Weighted ENO Schemes, J. Comput. Phys. 126 (1996) 202–228.
A. K. Henrick, T. D. Aslam, J. M. Powers, Mapped weighted essentially non-oscillatory schemes: Achieving optimal order near critical points, J. Comput. Phys. 207 (2005) 542–567.
A. D. Klose, U. Netz, J. Beuthan, A. H. Hielscher, Optical tomography using the time-independent equation of radiative transfer - Part 1 : forward model, J. Quant. Spectrosc. Radiat. Transfer 72 (2002) 691–713.

H. Fujii, S. Okawa, Y. Yamada, Y. Hoshi, Hybrid model of light propagation in random media based on the time-dependent radiative transfer and diffusion equations, J. Quant. Spectrosc. Radiat. Transfer 147 (2014) 145–154.

A. D. Klose, E. W. Larsen, Light transport in biological tissue based on the simplified spherical harmonics equations, J. Comput. Phys. 220 (2006) 441–470.

H. Fujii, S. Okawa, K. Nadamoto, E. Okada, Y. Yamada, Y. Hoshi, M. Watanabe, Numerical modeling of photon migration in human neck based on the radiative transport equation, Journal of Applied Nonlinear Dynamics 5 (2016) 117–125.

R. Kannan, A High Order Spectral Volume Formulation for Solving Equations Containing Higher Spatial Derivative Terms II : Improving the Third Derivative Spatial Discretization Using the LDG2, Commun. Comput. Phys. 12 (2012) 767–788.

S. Gottlieb, C.-W. Shu, Total variation diminishing Runge-Kutta schemes, Math. Comp. 67 (1998) 73–85.

H. Fujii, Y. Yamada, K. Kobayashi, M. Watanabe, Y. Hoshi, Modeling of light propagation in the human neck for diagnoses of thyroid cancers by diffuse optical tomography, Int. J. Numer. Meth. Biomed. Engng. 33 (2017) 1–12.

F. Kamran, O. H. A. Abildgaard, A. A. Subash, P. E. Andersen, S. Andersson-engels, D. Khoptyar, Computationally effective solution of the inverse problem in time-of-flight spectroscopy, Opt. Express 23 (2015) 6937–6945.

A. N. Bashkatov, E. A. Genina, V. V. Tuchin, OPTICAL PROPERTIES OF SKIN, SUBCUTANEOUS, AND MUSCLE TISSUES : A REVIEW, J. Innov. Opt. Health Sci. 4 (2011) 9–38.

S. Chandrasekhar, Stochastic Problems in Physics and Astronomy, Rev. Mod. Phys. 15 (1943) 1–88.

K. Furutsu, Y. Yamada, Diffusion approximation for a dissipative random medium and the applications, Phys. Rev. E 50 (1994) 3634–3640.